Journal of Imaging Science and Technology® 55(6): 060502-1–060502-14, 2011.

Spatio-Spectral Modeling and Compensation of Transversal Chromatic Aberrations in Multispectral Imaging[1]

Julie Klein▲, Johannes Brauers, and Til Aach
Institute of Imaging & Computer Vision, RWTH Aachen University, Templergraben 55, D-52056 Aachen, Germany
E-mail: julie.klein@lfb.rwth-aachen.de

Abstract. *In optical imaging systems, the wavelength-dependency of the refraction indices of lenses causes chromatic aberrations: electromagnetic radiation from an object point is dispersed in a rainbow-like manner on the sensor. These aberrations were so far only measured and modeled for up to three, often relatively wideband wavelength bands, such as R, G, and B. Moreover, no relation between the aberrations of these color channels was generally considered. The authors describe here the measurement of chromatic aberrations for multiple narrowband color channels in multispectral imaging. Existing models for transversal distortions are discussed and the wavelength-dependency of their parameters is analyzed. The models are extended with univariate wavelength-dependent polynomials, thus leading to bivariate models for both space and wavelength-dependency. The authors compare the models and confirm their validity qualitatively and quantitatively and simulate aberrations with state-of-the-art raytracing software. With their wavelength-dependent model, the distortions can be compensated even at wavelengths for which no measurements are available.* © *2011 Society for Imaging Science and Technology.*
[DOI: 10.2352/J.ImagingSci.Technol.2011.55.6.060502]

INTRODUCTION

Chromatic aberrations are caused by the wavelength-dependency of the refraction indices of glasses and are, therefore, almost unavoidable in any optical imaging system. The radiation of different wavelengths emitted by an object point is not propagated in the same way by the lenses, thus does not focus exactly on the same point and reaches the sensor plane at slightly different positions. The chromatic aberrations are divided into two categories: longitudinal ones, caused by the variation of the focus along the optical axis and resulting in a blurring of the image, and transversal ones,[1] caused by the wavelength-dependent displacement of the image points in the sensor plane and producing color fringes[2] (see Figure 1). In this work, we analyze the transversal chromatic aberrations.

Since chromatic aberrations appear in all color imaging systems, understanding their effects is quite important. This includes RGB as well as multispectral imaging systems. For the latter ones, examining the chromatic aberrations is particularly relevant since they allow a separation of the electromagnetic spectrum into narrow wavelength bands. Multispectral cameras use, for instance, a tunable filter or between 5 and 13 optical bandpass filters[3–11] to divide the electromagnetic spectrum into different passbands. These spectral filters allow the acquisition of as many color components as there are filters, each color component being represented by a grayscale image that corresponds to the wavelength band. The grayscale images are then combined to a multispectral image. We estimate the incident spectra from the color components via Wiener estimation[6,12] and transform them to an RGB image to enable their visualization on a computer monitor; other, more sophisticated methods may be used.[13] Because of the chromatic aberrations, the grayscale images are slightly shifted and blurred relative to each other. This causes color fringes when the different color channels, i.e., the different wavelength bands, are combined to a multispectral image. Multispectral systems may also encounter other aberrations, such as the filter induced aberrations discussed by Brauers et al.[12] Analyzing the chromatic aberrations separately allows a better modeling and a better compensation of each of them, and the output image contains thus less errors.

Chromatic aberrations have already been measured in prior work. Beads are simultaneously stained with three different narrowband fluorescent dyes, and the weight centers of these beads are used to measure the chromatic aberrations by Kozubek and Matula.[14] Edges of a pattern with known geometry are detected on three broadband color planes—the red, green, and blue color planes of an RGB camera—to estimate the chromatic aberrations.[15–17] Using the same three color planes, the detected edges can be the crossings of a checkerboard pattern.[18] However, the use of wideband color channels implies an integration of radiation over a large bandwidth and does not allow a wavelength specific analysis. In our case, we use much narrower color bands and increase the number of bands to seven.

Some models describing the lateral chromatic aberrations are also introduced in the literature. In some papers, the distortions are split into their horizontal and vertical components and then analyzed.[14,15] When analyzing chromatic aberrations independently for pairs of fluorochromes, these two components turn out to be almost linearly dependent on the position of the image point.[14]

[1]Parts of this work were presented at the IS&Ts 5th European Conference on Colour in Graphics, Imaging, and Vision (CGIV, June 14–17 2010, Joensuu, Finland).
▲IS&T Member.

Received Apr. 5, 2011; accepted for publication Nov. 3, 2011; published online Dec. 23, 2011
1062-3701/2011/55(6)/060502/14/$20.00.

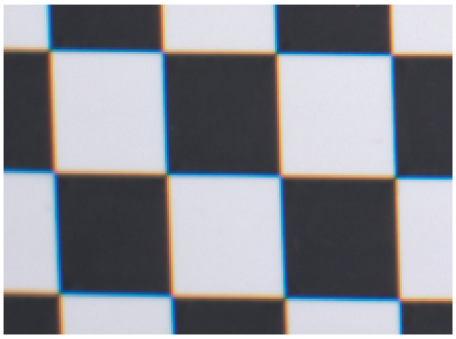

Figure 1. Color fringes on a black and white checkerboard pattern—only the bottom left corner of the image is displayed.

The two components can be approximated separately by a cubic spline for the two coordinates of the image point with chromatic aberrations measured between the reference color plane blue and the color planes red and green.[15] Joshi et al.[17] compute a radial correction in order to align the edges in the red and blue planes to the edges in the green plane, which is taken as reference plane. Radial and tangential distortion terms are introduced by Conrady[19] and Brown[20] and used by Mallon and Whelan[18]: the distortions of an image point in a color plane are calculated as a function of the corresponding image point from a reference color plane, being, for instance, the green color plane. An affine model, in which the displacements of an image point between two color channels are described by a rotation, a translation and a nonisotropic scaling,[12] can also be used.

In Refs. 21–23, the chromatic aberrations in digital RGB images are compensated using image processing, but no model of the distortions, which is what we aim at, is proposed. Transversal and longitudinal chromatic aberrations of single images are characterized by Kang,[24] by modeling the optics, the pixel sampling, and the in-camera postprocessing. This model as well as the previous ones consider the chromatic aberrations in each color plane separately, and no link between the planes is given. Here, we, therefore, analyze the chromatic aberrations over the whole set of narrowband color channels as a function of the wavelength bands and of the image position to derive a more general model. Since all presented models describe relative chromatic aberrations between two color planes, we also sought to avoid the use of any reference color plane or any reference image point. Moreover, we use a principal component analysis of the spectra of gray objects images to compare the first principal component at each pixel position: in the presence of chromatic aberrations, this spectrum can have any spectral composition, but after compensation of the chromatic aberrations, it should be a constant gray spectrum. The first principal component of compensated images of a gray object being a gray spectrum will thus confirm the accuracy of the models. Finally, we confirm the robustness of our wavelength-dependent model by compensating chromatic aberrations after incomplete calibration measurements.

In the following, we first describe how the chromatic aberrations appear, how they can be measured and how the distortions present in images can be compensated. We, then, derive models for the relative chromatic aberrations give results concerning the parameters of the models and calculate their accuracy. We also compare the measurements with simulated chromatic aberrations before we finish with conclusions.

PHYSICAL BACKGROUND

We consider an object point and its image formed on the sensor plane via the objective lens. Without any aberration, its image would be a single point. However, since the refraction indices of optical elements are wavelength-dependent, each spectral component of the object point is refracted differently in the lenses and finally reaches the sensor plane at a different position. The wavelengths composing the object point thus form a rainbow-like cloud of image points. For instance, the blue wavelength band is in general refracted stronger than the red one.[25] In our images, the image points corresponding to low wavelengths are therefore nearer to the optical axis, or, more precisely, the image center, than those corresponding to high wavelengths. This results in color fringes at lines and edges in the images, as shown in Fig. 1: here, the image points corresponding to blue wavelengths are nearer to the optical axis, which is situated toward the upper right of the displayed image part. This results in blue color fringes at the upper and right edges of the white squares. In the same way, there are red fringes at the bottom and left edges of the white squares.

The object points situated along the optical axis of the objective are not distorted by transversal chromatic aberrations: their lines of sight follow the optical axis for all wavelengths. Their image points are all located on the image center $(u_0, v_0)^T$, which is the point where the optical axis intersects with the sensor plane. This means that the rays on the optical axis are free of transversal chromatic aberrations and that the image center $(u_0,v_0)^T$ on the sensor is also the center of the transversal chromatic aberrations.

Measurement of Chromatic Aberrations

The chromatic aberrations can be measured by following one specific object point and its image points for different wavelengths. Since a continuous measurement over the entire visible spectrum is not feasible, the aberrations are only measured for discrete wavelength values. The specific object points we use are the crossings of a checkerboard pattern. These crossings are detected and their positions are determined with subpixel accuracy using the algorithm from Mühlich and Aach.[26] In relatively low-noise images such as ours, the crossings can be localized with an accuracy of 0.03 pixels.

To isolate the image points for different known wavelengths, we use spectral bandpass filters that enable us to allow only the rays of one wavelength band coming from the object point to pass through the lenses and to hit the sensor. We place the spectral filters in front of the light source, because filters placed in the optical path, i.e., between the object and the sensor, lead to additional aberrations as explained in Ref. 12, which we need to avoid. As shown in Figure 2, the scene is directly illuminated with the radiation of a wavelength band and only the radiation of this wavelength band arrives at the optical system (except in case of fluorescent paper where the wavelength band is slightly shifted, as explained in the next paragraph). With this experimental setup, each color component of the scene corresponding to each wavelength band is recorded separately on a grayscale image. Each object point is then projected to a different image point on the sensor plane, depending on the wavelength band.

The seven spectral filters we use are mounted in a filter wheel and have center wavelengths ranging from 400 to 700 nm in steps of 50 nm and bandwidths of 40 nm, see Fig. 2. Note, though, that the light irradiated onto the paper sheet with the checkerboard pattern may be reemitted with slightly different wavelengths due to fluorescence caused by optical brightener contained in the paper. This holds particularly for illumination wavelengths close to ultraviolet at about 400 nm. Although the paper we used is labeled "without any optical brightener" (GMG ProofPaper semimatte 250), it is still fluorescent. We measured the spectrum of the paper under the different illuminations and the central reemission wavelength of the color channel corresponding to the 400 nm filter is 418 nm. The center wavelengths λ_c of the color channels we used are thus 418, 450, 500, 550, 600, 650, and 700 nm.

The coordinates of the image points are denoted by $(u_c, v_c)^T$, where c represents the chosen color channel that corresponds to a particular wavelength band. In the following, we will use the relative coordinates $\mathbf{p}_c$ of the image points, which relate to the center of the distortions $(u_0, v_0)^T$: $\mathbf{p}_c = (x_c, y_c)^T = (u_c - u_0, v_c - v_0)^T$. Since the optics is not modified during the measurements, the center of the distortions $(u_0, v_0)^T$ remains the same for all the color channels.

One of the color channels is taken as a reference channel, and the chromatic aberrations are then calculated relative to this reference channel. The corresponding image points $\mathbf{p}_r = (x_r, y_r)^T$ in the reference channel and $\mathbf{p}_c$ in another color channel c are localized, and the relative distortions $\Delta\mathbf{e}_c$ in the color channel c are defined by

$$\Delta\mathbf{e}_c(\mathbf{p}_r) = \mathbf{p}_c - \mathbf{p}_r, \tag{1}$$

as shown in Figure 3. The aim of this work is the modeling of $\mathbf{p}_c$ or of $\Delta\mathbf{e}_c$, respectively, as a function of the image position $\mathbf{p}_r$ and of the color channel c, which corresponds to a certain wavelength λ_c.

Observations

The chromatic aberrations observed at the crossings of a checkerboard pattern using several different wavelength bands are shown in Figure 4(a). The wavelength-dependency of the lens is evident, since the distortions vary with the wavelength band. We selected the 700 nm channel as reference color channel. Fig. 4(a) depicts the displacements $\Delta\mathbf{e}_c(\mathbf{p}_r)$ from the crossings $\mathbf{p}_r$ in the reference channel to the crossings $\mathbf{p}_c$ in the other channels from 418 to 650 nm: the distortions exhibit a radial symmetry around the center of the chromatic aberrations. The displacements of the low wavelengths are stronger than those of the high wavelengths and they point toward the center of the chromatic aberrations. For each crossing of the checkerboard pattern, the displacements relative to the reference color channel exhibit approximatively the same direction, as shown in Fig. 4(b).

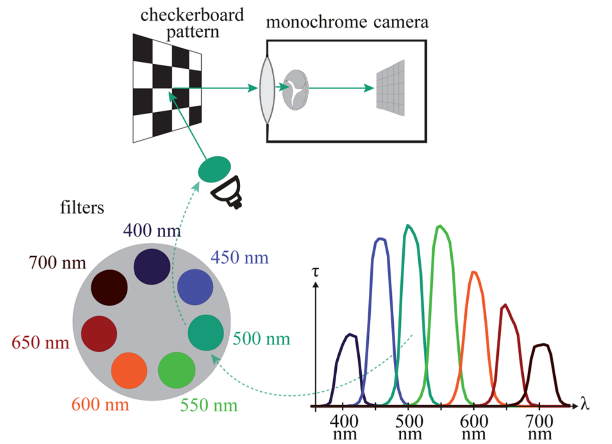

Figure 2. The experimental setup to measure chromatic aberrations. A checkerboard pattern is illuminated with radiation of a known wavelength band: a color bandpass filter with the transmittance curve $\tau(\lambda)$ is placed in front of the light source. The scene is then recorded with a monochrome camera. The characteristic curves of the seven color filters that are included in a filter wheel are shown in the lower right: their center wavelengths λ_c range from 400 to 700 nm in steps of 50 nm. Due to the fluorescence of the paper sheet, the center wavelength reemitted by the checkerboard pattern for the 400 nm filter is shifted to 418 nm.

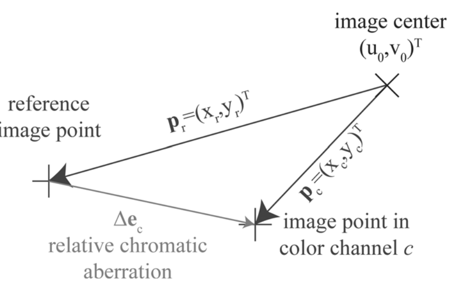

Figure 3. The image points corresponding to one object point have the positions $\mathbf{p}_r$ in the reference color channel and $\mathbf{p}_c$ in a color channel c, relative to the image center $(u_0, v_0)^T$. The chromatic aberration $\Delta\mathbf{e}_c(\mathbf{p}_r)$ of the color channel c for the image point $\mathbf{p}_r$ is the distance vector between both image points.

Simulation of the Aberrations

We also simulated the chromatic aberrations of a representative lens, details of which are described in the patent,[27] with the simulation software ZEMAX (Zemax Development Corporation, Bellevue, WA). This professional software enables to simulate all rays coming from an object point and arriving at the sensor plane with very high accuracy, thus providing a ground truth. With the simulation, we are

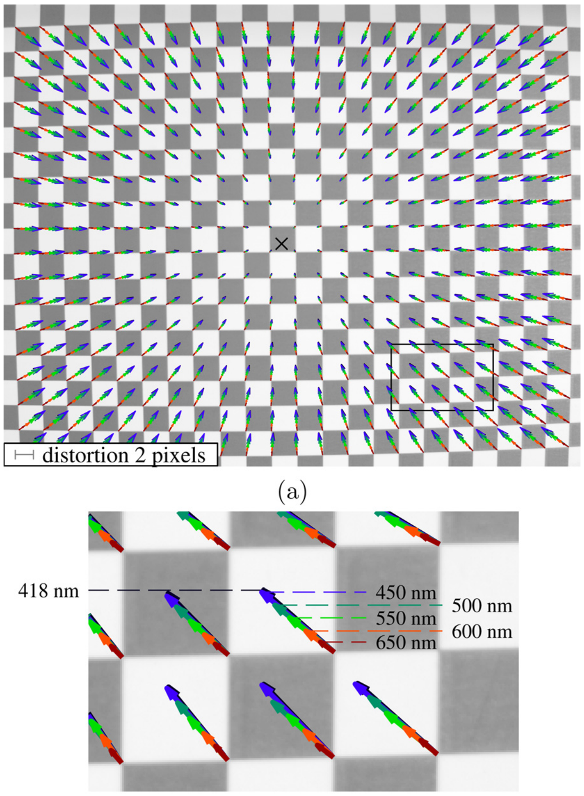

Figure 4. Chromatic aberrations observed by analyzing the crossings of a checkerboard pattern in an image of 1280 × 1024 pixels. The vectors show the distortions $\mathbf{p}_c - \mathbf{p}_r$ from the crossings $\mathbf{p}_r$ of a reference color channel to the crossings $\mathbf{p}_c$ of the other color channels with a 20 × magnification (a). The image center is represented by a black cross. The distortions of the crossings contained in the marked area are displayed in (b). The reference color channel is the wavelength band 700 nm, and the distortions for the other wavelength bands (418 to 650 nm) are color-coded.

independent of the crossing detection accuracy, image noise, and other practical issues. The objects at the entry of the optical system are isolated points placed at the crossings of a grid. We calculated the coordinates of their image points for the wavelengths 418, 450, 500, 550, 600, 650, and 700 nm. We, then, took the image points corresponding to the wavelength 700 nm as reference and calculated the relative distortions of the other color channels, as we did previously with the checkerboard pattern images. These simulated relative distortions displayed in Figure 5 are similar to those measured using the crossings of a checkerboard pattern (Fig. 4(a)): they point to the center of the chromatic aberrations and the image points near this center are less distorted than those situated on the edges of the image.

Compensation of the Chromatic Aberrations

Once the distortions have been measured, the color channels constituting the multispectral image can be corrected. Each spectral channel c is compensated separately so as to match the reference spectral channel. Since the compensated image of each spectral channel must be equidistantly sampled, the compensation starts with the final coordinates $\mathbf{p}_{c,\mathrm{comp}}$ of the compensated image that cover all pixels. The corresponding distorted coordinates $\mathbf{p}_{c,\mathrm{dist}}$ of the input image, i.e., of the distorted image of the color channel c, can then be traced back by inserting the measured distortions in Eq. (1). The pixel values of the positions $\mathbf{p}_{c,\mathrm{dist}}$ in the distorted image are calculated using a bilinear interpolation and are then transferred to the coordinates $\mathbf{p}_{c,\mathrm{comp}}$ in the final compensated image, as explained by Brauers and Aach.[28] All channels—except the reference channel—are processed separately in order to complete the compensation of the distortions in the multispectral image.

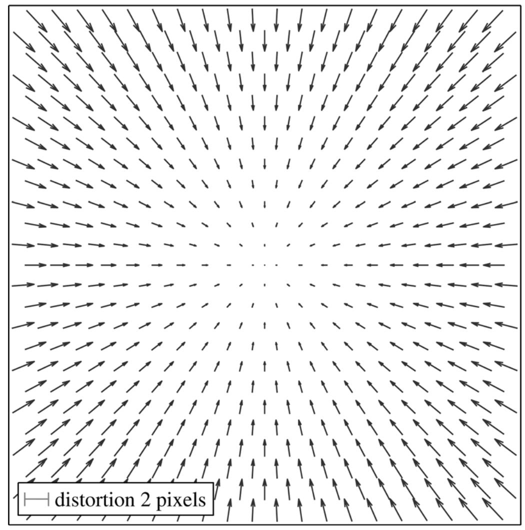

Figure 5. Simulated distortions of the wavelength band 450 nm for a 1700 × 1700 pixels image. This simulation is similar to the measured distortions shown in Fig. 4, now with a 40 × magnification. The lengths and orientations of the distortions are further examined in Fig. 16.

In addition to this *measurement-based* compensation of distortions, we will, in the following, use these measurements to also derive distortion models. Toward this end, we start out from an affine model, but as we will see, a sufficiently accurate description of the distortions requires a more sophisticated model accounting explicitly for both radial and tangential distortion components. We will show that this model can be generalized to include the wavelength-dependency of the distortions. Once the model parameters are estimated from the above calibration measurements, the distortions can be compensated in a *model-based* manner for other captured image data as well.

MODELING CHROMATIC ABERRATIONS

As mentioned in the section explaining the physical background, a reference color channel r is selected and the chromatic aberrations $\Delta\mathbf{e}_c$ of all other color channels c are defined relative to the reference channel. The chromatic aberrations of a color channel c are calculated using the image points $\mathbf{p}_r$ in the reference channel and the image points $\mathbf{p}_c$ in the channel c, see Eq. (1).

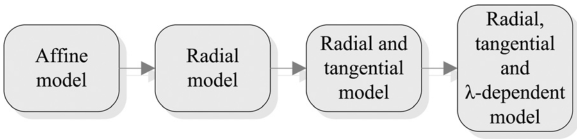

Figure 6. Step-by-step approach utilized in this paper to model the relative chromatic aberrations.

We investigate several ways to model either the coordinates $\mathbf{p}_c$ of the image points or the relative chromatic aberrations $\Delta\mathbf{e}_c$. We examine the role of the wavelength in the parameters of these models to finally develop a global model for the chromatic aberrations that take as free variables the positions in the image *and* the wavelengths.

Figure 6 illustrates our step-by-step approach: We begin by a straightforward affine model for the spatial distortions. As it will turn out, this model will not allow generalization toward wavelength-dependency. Based on the observations in Fig. 4, we, therefore, develop a more specific radial model for the distortions, which is then refined by also taking tangential distortions into account. The, thus, resulting radial and tangential model is then in a final step extended to include the wavelength-dependency of the distortions.

Affine Model

The relative chromatic aberrations are first modeled by a straightforward affine transformation. An affine transformation includes a rotation, a translation, and a nonisotropic scaling. The image point in the color channel c that is estimated using the affine model is called $\hat{\mathbf{p}}_c^{\mathrm{aff}}$. It is calculated by

$$\hat{\mathbf{p}}_c^{\mathrm{aff}} = \mathbf{T}_c \cdot \begin{pmatrix} \mathbf{p}_r \\ 1 \end{pmatrix}, \tag{2}$$

using the image point $\mathbf{p}_r$ in the reference channel and the matrix $\mathbf{T}_c \in^{2\times3}$. The translation is described by the elements $T_c(1, 3)$ and $T_c(2, 3)$, while the rotation and the nonisotropic scaling are described by the elements $T_c(1, 1)$, $T_c(1, 2)$, $T_c(2, 1)$, and $T_c(2, 2)$.

The estimated distortion $\Delta\mathbf{e}_c^{\mathrm{aff}} = \hat{\mathbf{p}}_c^{\mathrm{aff}} - \mathbf{p}_r$ caused by the chromatic aberrations is then computed by:

$$\Delta\mathbf{e}_c^{\mathrm{aff}}(\mathbf{p}_r) = \left(\mathbf{T}_c - \begin{pmatrix} 1 & 0 & 0 \\ 0 & 1 & 0 \end{pmatrix}\right) \cdot \begin{pmatrix} \mathbf{p}_r \\ 1 \end{pmatrix}. \tag{3}$$

As shown in the "Results" section, this straightforward model compensates a certain amount of the distortions but becomes inadequate for increasing distortions: it is not appropriate to model the chromatic aberrations over all pixels and all wavelengths. Moreover, the wavelength-dependency of the matrix coefficients $T_c(i, j)$, $1 \le i \le 2$, $1 \le j \le 3$, could for the six center wavelengths λ_c of the color channels not be approximated by an elementary function of λ, such as a low-order polynomial. The affine model was, therefore, not further investigated.

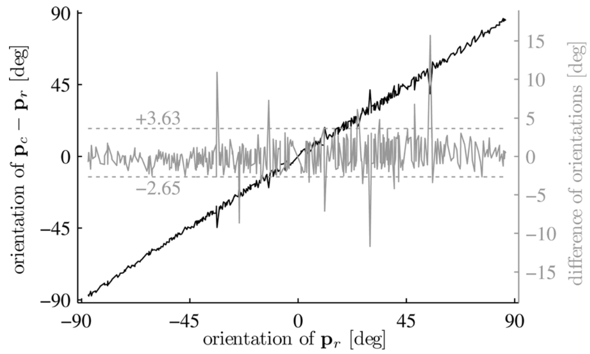

Figure 7. The orientations of the distortion vectors $\mathbf{p}_c - \mathbf{p}_r$ are displayed with respect to the orientations of the vectors $\mathbf{p}_r$ in black, and the differences of both orientations are displayed in gray. The orientations of $\mathbf{p}_c - \mathbf{p}_r$ and of $\mathbf{p}_r$ are quite similar: the maximum difference between them is 15.7° for some outliers in this color channel, while 95% of the differences lie between $-2.65°$ and $+3.63°$.

Radial Model

A first glance at the distortions of the crossings in Fig. 4(a) shows that the chromatic aberrations exhibit a prominent radial component. This is corroborated by Figure 7: the orientations of the measured distortion vectors $\mathbf{p}_c - \mathbf{p}_r$ are displayed in black as a function of the orientations of the vectors $\mathbf{p}_r$ pointing to the crossings, and their correspondence is quite good. The difference between both orientations is also displayed: for the color channel shown, the mean absolute difference is 1.54° and the maximum absolute difference is 15.7°. Over all channels, the mean absolute difference is 1.72° and the maximum difference is 33.8°. There are occasional outliers for which the difference of the orientations can reach 10° or more. These are mainly the crossings situated near the center of the chromatic aberrations, where any small error in the measured position of the center leads to large errors in the orientations of these crossings.

We, therefore, model only the radial components of the chromatic aberrations in this step. This means that for each crossing of the checkerboard pattern, its image point $\mathbf{p}_r$ in the reference color channel, its image point $\hat{\mathbf{p}}_c^{\mathrm{rad}}$ estimated using the radial model in another color channel c and the center of the chromatic aberrations are in line. Figure 8 shows the distortion $\| \mathbf{p}_c \| - \| \mathbf{p}_r \|$ between the points in the color channel c and the reference channel as a function of $\| \mathbf{p}_r \|$, where $\| \,.\, \|$ denotes the Euclidean norm. With the above approximation of vanishing tangential distortions, we have $|\|\mathbf{p}_c\| - \|\mathbf{p}_r\|| \approx \left\|\hat{\mathbf{p}}_c^{\mathrm{rad}} - \mathbf{p}_r\right\|$, where $\hat{\mathbf{p}}_c^{\mathrm{rad}}$ is the estimate of $\mathbf{p}_c$ using the radial model. In our case, $\mathbf{p}_c$ is closer to the center than $\mathbf{p}_r$, and the values $\| \mathbf{p}_c \| - \| \mathbf{p}_r \|$ are therefore negative. Our aim is to find a function

$$f_c(\|\mathbf{p}_r\|) = \|\mathbf{p}_c\| - \|\mathbf{p}_r\| \tag{4}$$

that describes the distortions displayed in Fig. 8.

By multiplying Eq. (4) with $\mathbf{p}_r/\| \mathbf{p}_r \|$ and inserting once $\mathbf{p}_r/\|\mathbf{p}_r\| = \mathbf{p}_c^{\mathrm{rad}}/\left\|\hat{\mathbf{p}}_c^{\mathrm{rad}}\right\|$ since the vectors $\mathbf{p}_r$ and $\hat{\mathbf{p}}_c^{\mathrm{rad}}$ point in the same direction, we obtain

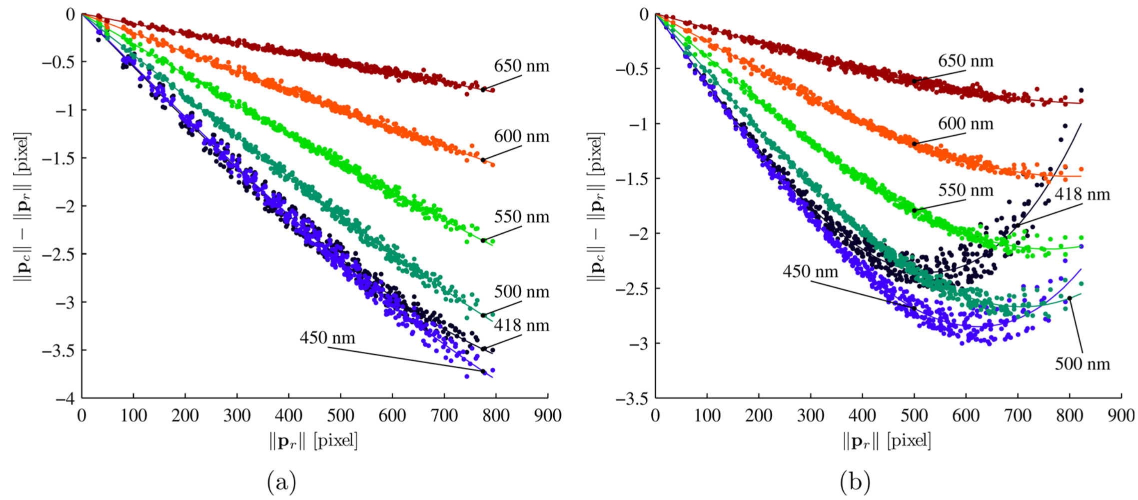

Figure 8. Distortions $\| \mathbf{p}_c \| - \| \mathbf{p}_r \|$ as a function of the distances $\| \mathbf{p}_r \|$ between the crossings and the center of the chromatic aberrations in the reference color channel. The measurements, represented by dots, were approximated by third-order polynomials according to Eq. (8), represented by lines. (a) and (b) are the measurements for two different lenses (Cosmicar and Tarcus, respectively). Information about the lenses is given in the "Results" section.

$$\frac{\mathbf{p}_r}{\|\mathbf{p}_r\|} f_c(\|\mathbf{p}_r\|) = \frac{\|\mathbf{p}_c\|}{\left\|\hat{\mathbf{p}}_c^{\text{rad}}\right\|} \hat{\mathbf{p}}_c^{\text{rad}} - \mathbf{p}_r. \tag{5}$$

Inserting $\|\mathbf{p}_c\| = \left\|\hat{\mathbf{p}}_c^{\text{rad}}\right\|$ yields finally for the estimation of the chromatic aberrations

$$\Delta\mathbf{e}_c^{\text{rad}}(\mathbf{p}_r) = \hat{\mathbf{p}}_c^{\text{rad}} - \mathbf{p}_r = f_c(\|\mathbf{p}_r\|) \frac{\mathbf{p}_r}{\|\mathbf{p}_r\|}. \tag{6}$$

Brown expresses the radial distortions[29] as

$$\begin{aligned} \mathbf{d}_{\text{rad}} &= \left(K_1\|\mathbf{p}_r\|^2 + K_2\|\mathbf{p}_r\|^4 + \ldots\right) \cdot \mathbf{p}_r \\ &= \left(K_1\|\mathbf{p}_r\|^3 + K_2\|\mathbf{p}_r\|^5 + \ldots\right) \cdot \frac{\mathbf{p}_r}{\|\mathbf{p}_r\|}, \end{aligned} \tag{7}$$

for positions $\mathbf{p}_r \neq (0, \ 0)^T$, with the parameters K_i, $i = 1,2,\ldots$. This means that the function f_c could be approximated using the powers 3,5,... of $\| \mathbf{p}_r \|$. However, our observations of the distortions $\| \mathbf{p}_c \| - \| \mathbf{p}_r \|$ as a function of the distances $\| \mathbf{p}_r \|$ in Fig. 8 do not lead to the same approximation. For some lenses, such as the Cosmicar lens (Fig. 8(a)), the function f_c is almost linear. For other lenses, such as the Tarcus lens (Fig. 8(b)), the measured values cannot be approximated by a linear function and a third-order polynomial is necessary, including the powers 1 and 2 of $\| \mathbf{p}_r \|$. In order to utilize as many parameters as required but also as few as possible, the function f_c is approximated by a third-order polynomial of $\| \mathbf{p}_r \|$

$$f_c(\|\mathbf{p}_r\|) \approx l_{c,1} \cdot \|\mathbf{p}_r\| + l_{c,2} \cdot \|\mathbf{p}_r\|^2 + l_{c,3} \cdot \|\mathbf{p}_r\|^3, \tag{8}$$

with specific coefficients $l_{c,i}$, $i = 1,\ldots,3$ for each color channel c. The coefficients $l_{c,i}$ correspond to the term of power i in the polynomial for the center wavelength λ_c of the cth color channel, λ_c being 418, 450, 500, 550, 600, or 650 nm. The coefficient corresponding to the term of power 0 in the polynomial is kept null, so that $f_c(\| \mathbf{p}_r \| = 0) = 0$ can be satisfied. For other types of lenses requiring more complex approximation, polynomials with higher order could be utilized.

We will now show that the *wavelength-dependency* of these coefficients can, in turn, be modeled parametrically, thus allowing to determine chromatic aberrations also for color channels with *other center wavelengths* than the ones above (see also the incomplete calibration in the "Results" section). To this end, we describe the wavelength-dependency of the coefficients $l_{c,i}$ by a function of the wavelength λ_c. Polynomial functions were tested and, because only 6 values are available for each coefficient, the order of these polynomials was restricted. From the values shown in Figure 11, a third-order polynomial with coefficients $m_{i,j}$, $j = 0,\ldots,3$, turned out to be sufficient for the approximation, yielding

$$l_{c,i} \approx m_{i,0} + m_{i,1} \cdot \lambda_c + m_{i,2} \cdot \lambda_c^2 + m_{i,3} \cdot \lambda_c^3, \tag{9}$$

where the order of the polynomial is as high as required and simultaneously as low as possible.

This model allows to calculate the coefficients of Eq. (8) for any wavelength λ between 418 nm and 650 nm, rather than only for the center wavelengths λ_c of the color channels. These coefficients extended to the whole wavelength range are denoted $l_i(\lambda)$ and are given by

$$l_i(\lambda) \approx m_{i,0} + m_{i,1} \cdot \lambda + m_{i,2} \cdot \lambda^2 + m_{i,3} \cdot \lambda^3. \tag{10}$$

By incorporating the coefficients $l_i(\lambda)$ into Eq. (8), the lengths of the distortions become $f(\lambda, \|\mathbf{p}_r\|)$, a function of the wavelength λ and of the distance $\| \mathbf{p}_r \|$ between the crossings in the reference color channel and the center of the chromatic aberrations. This generalizes the function $f_c(\| \mathbf{p}_r \|)$, which is only defined for discrete color channels. The function $f(\lambda, \| \mathbf{p}_r \|)$ is defined by 12 coefficients $m_{i,j}$, $i=1,\ldots,3$, $j=0,\ldots,3$:

$$f(\lambda, \|\mathbf{p}_r\|) = \sum_{i=1}^{3}\sum_{j=0}^{3} m_{i,j} \cdot \lambda^j \cdot \|\mathbf{p}_r\|^i. \tag{11}$$

As shown in the results (Figure 12), this model captures radial distortions almost perfect. However, a slight tangential error remains. The amplitude of these errors depends on the direction of the image point. In the “Radial and Tangential Model” section, we, therefore, take these tangential distortion components into account as well.

Radial and Tangential Model

The previously explained radial model relies on observations of the distortions. As illustrated in Fig. 3, there may additionally occur tangential components of the chromatic aberrations. For the radial and tangential model, we take three components into account: the radial distortions, the tangential distortions, and the effects of a linear dependency of the refraction index on the wavelength.[18] These three types of distortions can be found in the literature and are denoted $\mathbf{d}_{\mathrm{rad}}$, $\mathbf{d}_{\mathrm{tan}}$, and $\mathbf{d}_{\mathrm{lin}}$, respectively.

The radial distortions from Ref. 29 were already given in Eq. (7). When only the terms up to the third order of (x, y) are kept and the remaining coefficient is renamed, this model becomes

$$\mathbf{d}_{\mathrm{rad}} = n_2\|\mathbf{p}_r\|^2 \cdot \mathbf{p}_r, \tag{12}$$

where n_2 is a parameter for the spherical aberrations.[2] Decentering—or tangential—distortions were first introduced by Conrady[19] and then adopted by Brown,[20] which resulted in the Brown–Conrady model that classifies the lens distortions into radial and tangential distortions. The tangential ones[29] up to the third order of (x, y) are given by

$$\mathbf{d}_{\mathrm{tan}} = \begin{pmatrix} n_3(3x_r^2 + y_r^2) + 2n_4 x_r y_r \\ 2n_3 x_r y_r + n_4(x_r^2 + 3y_r^2) \end{pmatrix}, \tag{13}$$

with the coma parameters n_3 and n_4.[2] Another distortion term that does not appear in the two previous equations is also taken into account. This first-order term results from the linearity of the refraction index of lenses with respect to the wavelength within the visible spectrum[18] and is expressed as

$$\mathbf{d}_{\mathrm{lin}} = n_1 \cdot \mathbf{p}_r. \tag{14}$$

We use the three distortion terms from Eqs. (12)–(14) for each color channel and finally obtain the distortions $\Delta\mathbf{e}_c^{\mathrm{rtm}} = (\Delta e_{c,x}^{\mathrm{rtm}}, \Delta e_{c,y}^{\mathrm{rtm}})^T$ in the color channel c with the radial and tangential model that takes up to the third order of (x, y) into account

$$\begin{aligned} \Delta e_{c,x}^{\mathrm{rtm}}(\mathbf{p}_r) &= n_{c,1}x_r + n_{c,2}x_r\|\mathbf{p}_r\|^2 + n_{c,3}(3x_r^2 + y_r^2) \\ &\quad + 2n_{c,4}x_r y_r \\ \Delta e_{c,y}^{\mathrm{rtm}}(\mathbf{p}_r) &= n_{c,1}y_r + n_{c,2}y_r\|\mathbf{p}_r\|^2 + 2n_{c,3}x_r y_r \\ &\quad + n_{c,4}(x_r^2 + 3y_r^2). \end{aligned} \tag{15}$$

To each color channel c correspond specific parameters $n_{c,i}$, $i=1\ldots4$, that are used to determine the image point $\hat{\mathbf{p}}_c^{\mathrm{rtm}}$ with Eq. (1).

The parameter vector $\widehat{\theta}_c^{\mathrm{rtm}} = (u_0, v_0, n_{c,1}, n_{c,2}, n_{c,3}, 2n_{c,4})^T$ groups the six unknowns of the model. It is calculated by solving a nonlinear least squares problem where the model error, i.e., the difference between the estimated and the measured chromatic aberrations, is minimized with respect to the cost function $\left\|\Delta\mathbf{e}_c^{\mathrm{rtm}}(\mathbf{p}_r) - (\mathbf{p}_c - \mathbf{p}_r)\right\|^2$ which is a function of $\widehat{\theta}_c^{\mathrm{rtm}}$.[18] A Gauss–Newton method is used to find the solution of the nonlinear least squares problem by solving a sequence of linear least squares problem.[30] The parameter vector is first initialized, e.g., with $\widehat{\theta}_c^0 = (640, 512, 0, 0, 0, 0)^T$ for images of the size 1280×1024 pixels. An iteration loop then searches the parameter vector $\widehat{\theta}_c^{k+1}$ using the $\widehat{\theta}_c^k$ from the previous iteration until it converges: the cost function is linearized near $\widehat{\theta}_c^k$ and this linearized function is used as a cost function to find $\widehat{\theta}_c^{k+1}$.

Since the optical elements utilized (lens and sensor) were not modified during the measurements and only the wavelengths of the incoming rays were changed, the seven color channels we used had the same center for the chromatic aberrations. We, therefore, took into account that the two first elements of the vectors $\widehat{\theta}_c^{\mathrm{rtm}}$ should be the same for every channel c. The wavelength-dependency of this radial and tangential model is analyzed next.

Radial, Tangential and Wavelength-Dependen Model

The parameters $n_{c,i}$, $i=1,\ldots,4$, from the previous model are displayed separately in Figure 9 as functions of the wavelength. The six values $n_{c,i}$, with c corresponding to the color channels from 418 to 650 nm, which result from the optimization, are marked by points in each of the four subfigures. These six values can be approximated by third-order polynomials of the wavelength that represents the value of the parameter $n_{\lambda,i}$ for any wavelength λ between 418 and 650 nm (see the solid gray lines in the figure).

Once it has become clear that the parameters $n_{c,i}$ can be expressed as functions of the wavelength, this wavelength-dependency is used further and directly included in the definition of the model. The model becomes also wavelength-dependent.

To include the wavelength-dependency in the optimization, the parameters $n_{c,i}$, $i=1,\ldots,4$, are first approximated by third-order polynomials of the wavelength

$$n_{c,i} \approx n_i(\lambda_c) = q_{i,0} + q_{i,1} \cdot \lambda_c + q_{i,2} \cdot \lambda_c^2 + q_{i,3} \cdot \lambda_c^3, \tag{16}$$

similarly to Eq. (9). The coefficients $q_{i,j}$, $j=0,\ldots,3$, correspond to the jth power of the approximation of the

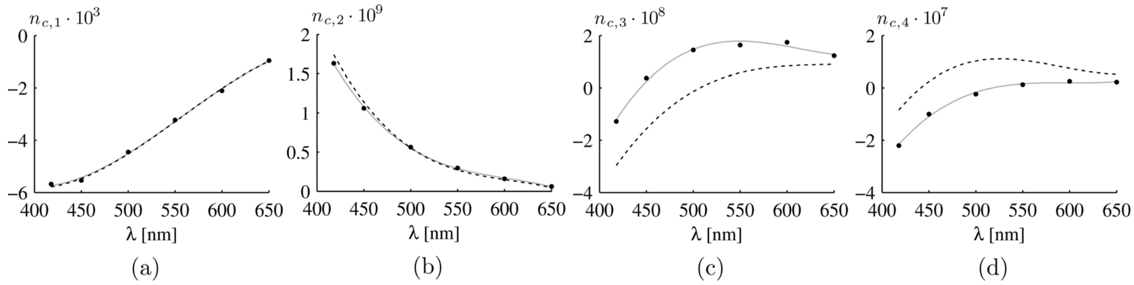

Figure 9. Values of the parameters from Eq. (15). The results of the optimization from the radial and tangential model are represented by points. They can be approximated by third-order polynomials (the solid gray lines), which generalizes the model for the entire wavelength range between 418 and 650 nm. The dotted black lines are the results of the global model, where the parameter estimation is performed for all image points and wavelengths at once.

parameter $n_{c,i}$. The chromatic aberration $\Delta\mathbf{e}^{\mathrm{wl}} = (\Delta\mathbf{e}_x^{\mathrm{wl}}, \Delta\mathbf{e}_y^{\mathrm{wl}})^T$ of this model then becomes a function of the wavelength λ (and not only of the center wavelengths λ_c but also of the color channels) and of the position $\mathbf{p}_r$ of the image point in the reference color channel. The distortion is described by a set of 16 coefficients $q_{i,j}$, $i = 1,\ldots,4$, $j = 0,\ldots,3$

$$\begin{aligned}
\Delta e_x^{\mathrm{wl}}(\lambda, \mathbf{p}_r) = {} & (q_{1,0} + q_{1,1}\lambda + q_{1,2}\lambda^2 + q_{1,3}\lambda^3)x_r \\
& + (q_{2,0} + q_{2,1}\lambda + q_{2,2}\lambda^2 + q_{2,3}\lambda^3)x_r\|\mathbf{p}_r\|^2 \\
& + (q_{3,0} + q_{3,1}\lambda + q_{3,2}\lambda^2 + q_{3,3}\lambda^3)(3x_r^2 + y_r^2) \\
& + 2(q_{4,0} + q_{4,1}\lambda + q_{4,2}\lambda^2 + q_{4,3}\lambda^3)x_r y_r \\
\Delta e_y^{\mathrm{wl}}(\lambda, \mathbf{p}_r) = {} & (q_{1,0} + q_{1,1}\lambda + q_{1,2}\lambda^2 + q_{1,3}\lambda^3)y_r \\
& + (q_{2,0} + q_{2,1}\lambda + q_{2,2}\lambda^2 + q_{2,3}\lambda^3)y_r\|\mathbf{p}_r\|^2 \\
& + 2(q_{3,0} + q_{3,1}\lambda + q_{3,2}\lambda^2 + q_{3,3}\lambda^3)x_r y_r \\
& + (q_{4,0} + q_{4,1}\lambda + q_{4,2}\lambda^2 + q_{4,3}\lambda^3)(x_r^2 + 3y_r^2).
\end{aligned} \tag{17}$$

The coordinates of the center of the chromatic aberrations $(u_0, v_0)^T$ and these 16 parameters $q_{i,j}$ form the vector $\widehat{\boldsymbol{\theta}}^{\mathrm{wl}}$ that describes the model of the aberrations over the whole wavelength range: $\widehat{\boldsymbol{\theta}}^{\mathrm{wl}} = (u_0, v_0, \{q_{i,j}\}_{i=1,\ldots,4, j=0,\ldots,3})^T$.

The parameter vector $\widehat{\boldsymbol{\theta}}^{\mathrm{wl}}$ can then be calculated, such as the parameter vector $\widehat{\boldsymbol{\theta}}^{\mathrm{rtm}}$ in the radial and tangential model, i.e., by minimizing a quadratic cost function using a Gauss–Newton scheme. The difference here is that the cost function takes the model errors for all the color channels into account at once and not for each color channel separately. The advantage of this model is that all the parameters are optimized simultaneously and that the chromatic aberrations can be estimated for *any* wavelength λ, even if it is not the center wavelength of one of the color channels. The results of the optimization are shown in Fig. 9: the dotted black lines are the third-order polynomial using the optimized coefficients $q_{i,j}$. The values are quite comparable to those from the radial and tangential model, especially for the lower order terms.

Absolute Chromatic Aberrations

A model for the absolute chromatic aberrations, i.e., a model giving the coordinates $\mathbf{p}_c$ of the distorted image points for each color plane c without using any reference color plane, would enable the entire correction of the chromatic aberrations without taking any color channel as a reference. One consideration is to model the coordinates $\mathbf{p}_c$ with respect to the coordinates $\mathbf{p}_u$ of the undistorted image points, which are the image points without any aberrations that result from pinhole projection.

Such models for camera calibration giving the undistorted image points are derived in Refs. 31 and 32. The camera is modeled using extrinsic and intrinsic parameters: the extrinsic parameters are the rotation and translation coefficients describing the transformation between the 3D coordinate systems of the object and of the camera, and the intrinsic parameters describe the transformation between the 3D coordinate system of the camera and the 2D coordinate system of the computer image. Regardless of whether a normalized image plane is used[32] or not[31] for this latter transformation, the intrinsic parameters include the effective focal length of the camera, the coordinates of the center of the image and coefficients corresponding to the pixel size.

The utilization of the models from Tsai[31] and Forsyth and Ponce[32] on calibration images illuminated with a specific wavelength band can thus provide the undistorted image point coordinates $\mathbf{p}_u$. These points are, e.g., computed by mathematically projecting three-dimensional points of a checkerboard pattern to the image plane by a pinhole model. However, since the refraction indices of the lens are wavelength-dependent, the effective focal length, e.g., is wavelength-dependent too. This means that the undistorted image point coordinates $\mathbf{p}_u$, which are computed using—among other parameters—the focal length also depend on the wavelength. Therefore, there is no single *undistorted* image point, which is valid for all spectral channels. These camera models are not appropriate to find any undistorted image point common to all spectral channels and thus are not appropriate to deduce a model for the absolute chromatic aberrations.

RESULTS

The effects of the chromatic aberrations on multispectral images of a gray and of a color object are shown in Figure 10. The scenes are recorded with the same experimental

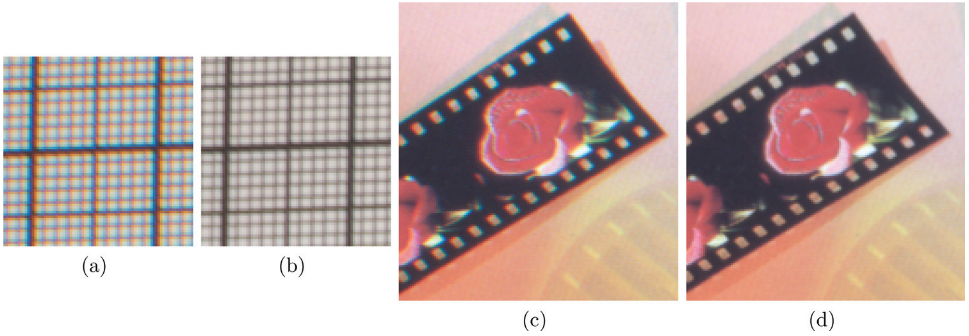

Figure 10. Initial images of a gray object (a) and a color object (c) with chromatic aberrations and results of the compensation of these distortions using the radial, tangential, and wavelength-dependent model (b), (d). The bluish and reddish fringes due to the chromatic aberrations are clearly visible at the sharp edges in the uncompensated images.

setup as the previously acquired checkerboard patterns, and the spectra of the objects are estimated using the seven color channels.[6,12] As explained before, color fringes appear, and they are especially noticeable near edges of the objects. The color fringes are more visible on sharp edges such as the black lines of a millimeter paper (Fig. 10(a)) or the perforations of the film and the edges of the petals in Fig. 10(c). To compensate these chromatic aberrations, we take a multispectral image of a checkerboard pattern with the same optical system in order to calculate the parameters of the models for the system. After that, we use these parameters to compensate the distortions. As Figs. 10(b) and 10(d) show the fringes then vanish completely. Since the distortions depend only on the position of the reference image point on the sensor (see Eqs. (3), (11), (15), and (17)), i.e., on the angles of the rays arriving at the optical system but not on the object distances, the models can also be utilized for natural scenes in which the objects are not planar and are positioned at different distances from the imaging device.

Our monochrome camera is an IDS uEye UI2240 CCD camera with a chip size of 7.60 mm $\times$ 6.20 mm and a resolution of 1280 $\times$ 1024 pixels. We use a Tarcus TV Lens 8 mm F1.3 and a Cosmicar TV Lens 8.5 mm F1.5.

Evaluation of the Model Parameters on Real Data

In the radial model, the distortions in the spectral channel c can be described by third-order polynomials of $\| \mathbf{p}_r \|$ with the coefficients $l_{c,i}$, $i = 1,\ldots,3$, as shown in Eq. (8). The coefficients corresponding to a given power, i.e., the values $l_{c,i}$ for a given i, are considered as a function of the channel center wavelength λ_c and are displayed in Fig. 11. This figure shows that the points $l_{c,i}$, $i = 1,\ldots,3$, can in their turn be approximated by third-order polynomials $l_i(\lambda)$ of the wavelength, represented by gray lines in the figure.

These continuous representations $l_i(\lambda)$ of the discrete coefficients $l_{c,i}$ are valid for the whole wavelength range from 418 to 650 nm, and ideally we have $l_i(\lambda_c) = l_{c,i}$. The results of the approximations are given in Table I. The radial model, which only uses the approximated lengths of the distortion and assumes that the distortion is radial, can thus be integrated into a model in which the distortions are a function of *both* the wavelength *and* the distance to the distortion center, as defined in Eq. (11).

The errors of the radial model, i.e., the difference between the measured relative chromatic aberrations and the modeled ones, are displayed in Fig. 12. The errors only have tangential components, which means that the approximation of the radial components was quite good. These tangential errors are taken into account in the radial and tangential model. The parameters $n_{c,i}$, $i = 1\ldots4$, of the radial and tangential model calculated for the utilized optical system are shown in Fig. 9, with the gray lines corresponding to their approximation using a third-order polynomial of the wavelength. Considering the approximated values (gray lines) instead of the calculated ones (dots) gave practically the same results and the errors remained almost the same.

In the next step, we directly include this wavelength-dependency into the optimization for the radial, tangential, and wavelength-dependent model by approximating the coefficients $n_{c,i}$ with a third-order polynomial of the wavelength (see Eq. (16)). The validity of the wavelength-dependency of the model was confirmed by the errors that remained almost the same as those of the preceding step (in which the coefficients $n_{c,i}$ were optimized and *then* approximated by a polynomial). The resulting polynomials $n_i(\lambda)$, $i = 1\ldots4$, define the coefficients for the *whole* wavelength range, in the same manner as $l_i(\lambda)$ previously. They are given in Table II for the used optical system. In this model, the chromatic aberrations become a function of *both* the wavelength *and* the position of the image point in the reference color channel.

The coefficients $n_{c,i}$ shown in Fig. 9 do not have the same values for the radial and tangential model (see the black dots) and for the radial, tangential, and wavelength-dependent model (see the dashed lines). The centers $(u_0, v_0)^T$ of the chromatic aberrations calculated with these two models are of course different, too. The modeled centers are $(636.55, 530.97)^T$ for the radial and tangential model and $(640.02, 511.98)^T$ for the radial, tangential, and wavelength-dependent model. The center of the latter

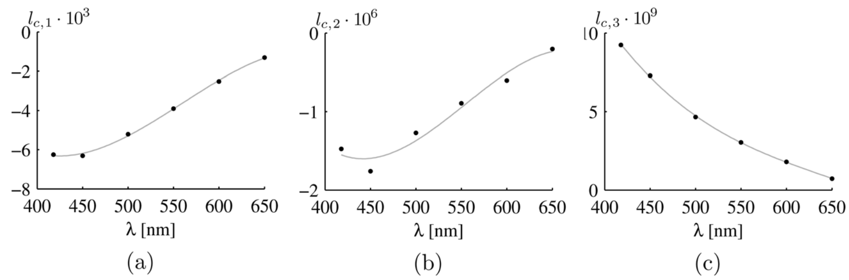

Figure 11. The wavelength-dependency of the parameters for the radial model in Eq. (8). The black points are the coefficients $l_{c,i}$, $i = 1,\ldots,3$ of Eq. (8), for $\lambda_c \in \{418\,\text{nm}, 450\,\text{nm}\ldots 650\,\text{nm}\}$. These values are then approximated by a third-order polynomial of the wavelength λ (see Eq. (9)). The polynomials are represented by gray curves and give the values $l_i(\lambda)$ for any λ between 418 and 650 nm.

Table I. Approximation of the coefficients for the radial model in Eq. (8) with third-order polynomials of the wavelength.

$l_1(\lambda) \cdot 10^3$	$=$	$7.522 \cdot 10 - 4.824 \cdot 10^{-1} \cdot \lambda$
		$+ 9.153 \cdot 10^{-4} \cdot \lambda^2 - 5.452 \cdot 10^{-7} \lambda^3$
$l_2(\lambda) \cdot 10^6$	$=$	$3.556 \cdot 10 - 2.160 \cdot 10^{-1} \cdot \lambda$
		$+ 4.064 \cdot 10^{-4} \cdot \lambda^2 - 2.445 \cdot 10^{-7} \lambda^3$
$l_3(\lambda) \cdot 10^9$	$=$	$1.061 \cdot 10^2 - 4.528 \cdot 10^{-1} \cdot \lambda$
		$+ 6.765 \cdot 10^{-4} \cdot \lambda^2 - 3.527 \cdot 10^{-7} \cdot \lambda^3$

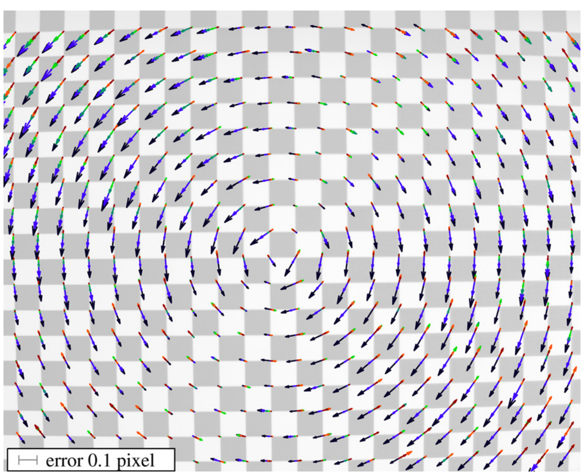

Figure 12. Errors of the radial model for all spectral channels on a 1280 × 1024 pixels image, with the same color code as in Fig. 4 and with a 400 × magnification. The errors exhibit evidently only a tangential component, which is not accounted for in the model. They are very small for the crossings situated in one particular direction (about 70°) and larger in the perpendicular direction.

model is closer to the position $(640, 512)^T$ used for the initialization of the optimization. The reason may be that the center of the chromatic aberrations represent 2/6 of the parameters for the radial and tangential model and only 2/18 of the parameters for the radial, tangential, and wavelength-dependent model, and the initial values are thus less modified in this model.

Table II. Approximation of the coefficients in Eq. (15) for the radial, tangential, and wavelength-dependent model.

$n_1(\lambda) \cdot 10^3$	$=$	$4.309 \cdot 10^1 - 3.013 \cdot 10^{-1} \cdot \lambda$
		$+ 5.884 \cdot 10^{-4} \cdot \lambda^2 - 3.527 \cdot 10^{-7} \lambda^3$
$n_2(\lambda) \cdot 10^9$	$=$	$4.346 \cdot 10^1 - 2.107 \cdot 10^{-1} \cdot \lambda$
		$+ 3.445 \cdot 10^{-4} \cdot \lambda^2 - 1.893 \cdot 10^{-7} \cdot \lambda^3$
$n_3(\lambda) \cdot 10^8$	$=$	$- 8.872 \cdot 10^1 + 4.194 \cdot 10^{-1} \cdot \lambda$
		$- 6.555 \cdot 10^{-4} \cdot \lambda^2 + 3.423 \cdot 10^{-7} \cdot \lambda^3$
$n_4(\lambda) \cdot 10^7$	$=$	$- 1.094 \cdot 10^2 + 5.737 \cdot 10^{-1} \cdot \lambda$
		$- 9.835 \cdot 10^{-4} \cdot \lambda^2 + 5.554 \cdot 10^{-7} \cdot \lambda^3$

Accuracy of the Models for Real Acquisition

The accuracy of the models is estimated using three approaches. First, the initial distorted image is visually compared to the images resulting from the compensation. Second, the errors in pixels between the estimated and the measured positions of the crossings of the checkerboard pattern are calculated. Third, the accuracy is assessed using a principal component analysis of the spectra in images of gray objects.

The visual comparison of parts of distorted and compensated images is shown in Fig. 10. Color fringes are present in the initial images (see Figs. 10(a) and 10(c)) and particularly visible at the sharp edges between dark and bright regions. A compensation of the chromatic aberrations with one of the models previously explained makes these color fringes disappear (see Figs. 10(b) and 10(d)). All the models seem to perform a good compensation of the chromatic aberrations, but their accuracy cannot be estimated quantitatively using this visual approach.

The calculation of the pixel errors for each model allows a better comparison of the model accuracies. For each color plane c, the distances $\left\|\mathbf{p}_c - \hat{\mathbf{p}}_c^{\text{model}}\right\|$ between the crossings $\mathbf{p}_c$ detected on the checkerboard and their estimates $\hat{\mathbf{p}}_c^{\text{model}}$ using the model are calculated. The mean and maximum values of these distances for each model are then compared in Figure 13. Evidently, the mean errors (solid lines in the figure) of the different models are quite close to each other: they lie between 0.019 and 0.062 pixel for

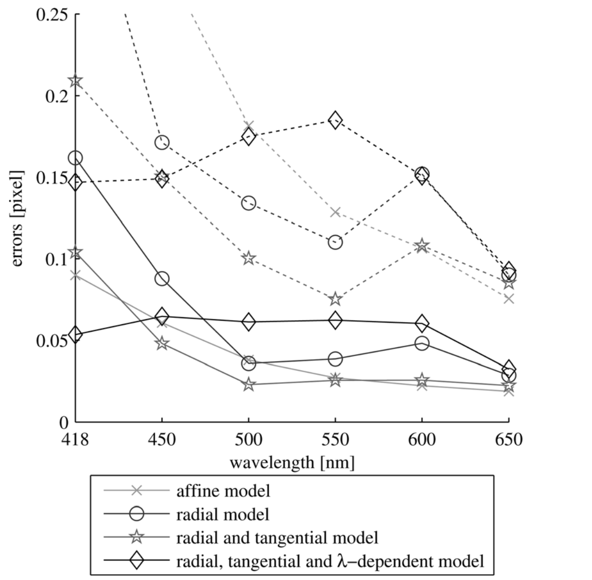

Figure 13. Errors of the implemented models for each wavelength band. They are calculated using the distance between a measured crossing $\mathbf{p}_c$ in a color channel and the corresponding crossing $\hat{\mathbf{p}}_c^{\text{model}}$ estimated by one of the models. The solid lines represent the mean errors over all crossings and the dashed lines are the maximum errors.

the channels from 500 to 650 nm. For the channels 418 and 450 nm, they become higher (between 0.048 and 0.162 pixels). There is only one model for which the mean errors do not increase for these two channels: the radial, tangential, and wavelength-dependent model, whose errors remain stable. The reason may be the global optimization of the parameters of this model that is performed over all wavelength bands. A parameter set leading to high errors for individual color channels would not be selected by this global optimization, although the utilization of the wavelength-dependency in a model that has already been optimized could result in outliers, as it is the case for the radial model and for the radial and tangential model. As the maximum errors show (dashed lines in Fig. 13), the affine model is not very precise for the increasing aberrations at lower wavelengths, such as in the color channels 418 and 450 nm: the maximum errors are above 0.28 pixels. The radial model also fails to describe the chromatic aberrations for the color channel 418 nm with a maximum error of about 0.35 pixels. The maximum errors over all color channels for the other models are 0.209 pixels for the radial and tangential model and 0.185 pixels for the radial, tangential, and wavelength-dependent model. The latter model is the one with the lowest maximum error, when the entire error over all the color channels is considered.

We employ principal component analysis (PCA) on images of gray objects to assess the potential occurrence of color fringes: the first principal component of an image containing only gray pixels should be a flat spectrum, since each gray pixel has a spectrum constant over the visible spectrum range. The eigenvalues corresponding to the other principal components should vanish. A nonconstant first principal component or large eigenvalues for the other principal components indicate that colors are present. The PCA makes the reduction of the dimensionality of a dataset possible by using a new coordinate system suited to the dataset. Starting from the initial coordinate system, a new coordinate system, whose axes are called principal components and which are expressed in the initial coordinate system, is calculated.[33] Its principal components are sorted so that the variance of the data that are projected onto these axes becomes smaller, and the PCA thus minimizes the energy contribution of the last components of the data in the new coordinate system.[34,35] For pure gray level images, the seven color channels will for each pixel exhibit the same value. A PCA on this data thus leads to a first principal component consisting of seven equal values as well, while the eigenvalues for the other principal components are null.

We perform a PCA on the initial uncompensated image of a gray millimeter paper (Fig. 10(a)), where color fringes are visible due to the chromatic aberrations. It is not surprising that the first component of this PCA does not exhibit seven equal values, as shown in Figure 14. The variances (eigenvalues) of the uncompensated image along the seven sorted principal components are shown in Figure 15 (black solid line). The variance of the data along the second principal component is almost the same as along the first one. This proves that the initial image is far from containing only gray pixels. We also perform a PCA on compensated images of the millimeter paper. The models for the relative chromatic aberrations we described previously all lead to similar first principal components composed of almost equal values, as shown in Fig. 14. The energy contribution of the first principal component of the compensated images is 98.4% for the affine model, 98.7% for the radial model, 98.5% for the radial and tangential model, and 98.5% for the wavelength-dependent model: they only vary by 3‰ and the radial model is best by very low margin. Moreover, even the second principal component is already way less important that the first one, since the eigenvalues of the second component are more than 100 times smaller than those of the first component in Fig. 15. The results of the PCA of the compensated images are thus close to those of the PCA of a perfect gray image and the compensations we performed led to similarly good gray images.

Aberrations Measured with Simulation

After the evaluation of the parameters and the accuracy of the models developed in the two previous subsections "Evaluation of the model parameters on real data" and "Accuracy of the models for real acquisition", we will now discuss the chromatic aberrations simulated with the ray-tracing software. The simulated aberration vectors $\mathbf{p}_c - \mathbf{p}_r$ have the same orientations as the corresponding crossings $\mathbf{p}_r$, as shown in Figure 16(a). The difference between the orientations of the crossings and those of the distortions remains below $9.3 \cdot 10^{-11}$ degrees for all color channels, and even below $4.1 \cdot 10^{-11}$ degrees for the color channel shown here. This means that the simulated chromatic

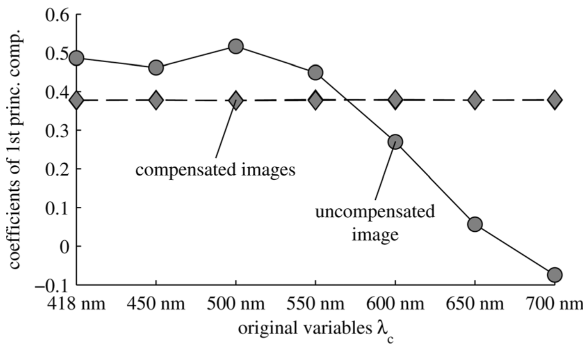

Figure 14. Coefficients of the first principal component of the colors present in the initial and in the compensated images of an object containing only gray values. The coefficients are expressed for the original variables λ_c, the center wavelengths of the color channels.

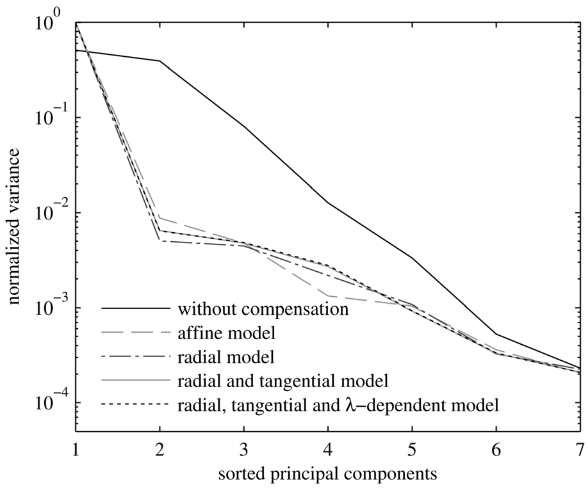

Figure 15. Variances of the data along each of the seven sorted principal components for the uncompensated image (black line) and for the images compensated with the four described models. The variances are normalized so that the sum over the seven principal components for one data set is one.

aberrations only have a radial component and the lengths $\| \mathbf{p}_c - \mathbf{p}_r \|$ are thus equivalent to the lengths $|\| \mathbf{p}_c \| - \| \mathbf{p}_r \||$. The relation between the distances $\| \mathbf{p}_r \|$ from the crossings $\mathbf{p}_r$ to the center of the chromatic aberrations and the values $\| \mathbf{p}_c \| - \| \mathbf{p}_r \|$ of the radial distortions are shown in Fig. 16(b). They are similar to the measured values displayed in Fig. 8 and can also be approximated by third-order polynomials.

For our experiments, we were able to limit the radiation of the light source to narrow (40 nm bandwidth) but not infinitesimal small passbands. The analysis of individual wavelengths is, however, possible for the simulation. While we are thus not able to genuinely measure the distortions for all wavelengths experimentally, the similar results of the measurements and the simulations confirm that our approach is valid. The wavelength-dependent models we deduced for wavelength bands should thus be also valid for individual wavelengths. Due to the specific simulated lens, the radial model here works better, but all the maximum errors between the simulated and the estimated image points lie below 0.121 pixel.

Compensation Using Incomplete Calibration Data

We tested the robustness of the radial, tangential, and wavelength-dependent model with respect to the wavelengths used for the measurement and calibration step. Indeed, when the wavelength-dependent model is correct, it is possible to measure the chromatic aberrations on just some of the color channels and calculate the aberrations for all the color channels.

In the section concerning the models accuracy, the results of the compensation with a *complete calibration* were exposed, that is, with all the six color channels being measured to calculate the parameters of the models. Here, we will show how the errors of the compensation are

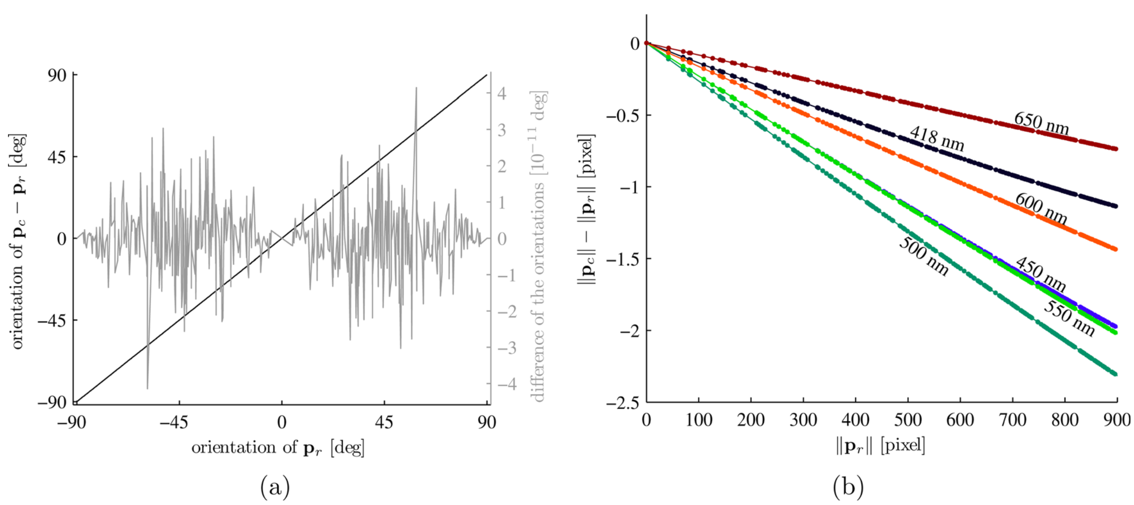

Figure 16. Orientations (a) and lengths (b) of the simulated distortions. The orientations of $\mathbf{p}_c - \mathbf{p}_r$ are almost equal to those of $\mathbf{p}_r$, since the maximum difference between both orientations is in the range of the machine accuracy for the color channel 450 nm displayed in (a). The lengths $\| \mathbf{p}_c \| - \| \mathbf{p}_r \|$ correspond to the lengths of the simulated chromatic aberrations, as the distortions are only radial. These lengths can be expressed as a third-order polynomial of the distance $\| \mathbf{p}_r \|$ for each wavelength (b).

Table III. Pixel errors of the compensation of chromatic aberrations using the radial, tangential, and wavelength-dependent model with a complete calibration data (the calibration is performed utilizing the six color channels) and with an incomplete calibration data (the calibration is performed without the color channel 500 nm). The errors are calculated on each color channel separately, and the mean and maximum errors values are multiplied by 100 and 10, respectively.

		Color channels					
Pixel error	Calibration data	418 nm	450 nm	500 nm	550 nm	600 nm	650 nm
Mean value × 100	Complete	5.346	6.465	6.131	6.232	6.030	3.241
	Incomplete	4.987	4.715	8.020	7.049	6.276	3.234
Maximum value × 10	Complete	1.468	1.489	1.749	1.849	1.507	0.928
	Incomplete	1.350	1.172	2.458	2.166	1.541	0.925

modified when an *incomplete calibration* is performed. We only utilized five out of the six color channels to measure the chromatic aberrations and left the color channel with the center wavelength 500 nm aside. We thus calculated the functions $n_i(\lambda)$, $i = 1 \ldots 4$, using exclusively the measurements on the color channels 418, 450, 550, 600, and 650 nm.

Table III shows the mean and the maximum pixel errors obtained with these two calibrations. The errors are calculated as they were for Fig. 13: the distance between the position of the crossings estimated with the model and the real ones are measured. As expected, the pixel errors for the color channel 500 nm that was not used for the calibration are larger: 0.08020 pixels with the incomplete calibration instead of 0.06131 with the complete calibration for the mean error. This represents an increase of 30% for the mean value of the pixel error. Still, the mean error remains low (about 0.08 pixels at the most), which could not be obtained without a wavelength-dependent model. For the neighbor color channel 550 nm, the errors were also slightly larger than with the complete calibration. For the color channels 600 and 650 nm, the results remain stable with the incomplete data set. The pixel errors even decreased for the color channels 418 and 450 nm. The wavelength-dependency of this model thus makes the estimation more robust: even with a missing measurement, all the color channels can be compensated with a good accuracy.

CONCLUSIONS

We have measured relative transversal chromatic aberrations for seven narrowband wavelength bands by illuminating a checkerboard pattern with narrowband radiation of a light source. The chromatic aberrations measured between two color channels with our lenses amounted to as much as 3.5 pixels. We used several existing models to describe the distortions and analyzed the parameters of these models and their wavelength-dependency: it turned out that the parameters can be approximated by third-order polynomials with respect to the wavelength. We, furthermore, directly included the wavelength-dependency into an existing model, which thus computes the relative transversal chromatic aberrations as a function of both the wavelength and the position in the image. All its parameters can then be optimized jointly by using all calibration coordinates from all spectral channels. We also simulated chromatic aberrations for the center wavelengths of our color channels, and the results are similar to those obtained with the wavelength bands, thus indicating that the models can also be applicable to individual wavelengths. The principal component analysis we performed on images of a gray object that are compensated with the presented models showed that the compensated images are almost only gray, i.e., free of color fringes: images containing chromatic aberrations can be compensated so that no visible color fringes remain. With our wavelength-dependent model, the distortions are calculated with a model error lower than 0.1849 pixels and even lower than 0.2458 pixels in case of incomplete calibration measurement.

ACKNOWLEDGMENTS

The authors acknowledge gratefully funding by the German Research Foundation (DFG, Grant No. AA 5/2 – 1).

REFERENCES

[1] H. Gross, H. Zügge, M. Peschka, and F. Blechinger, *Handbook of Optical Systems, Volume 3: Aberration Theory and Correction of Optical Systems* (Wiley-VCH Verlag GmbH & Co., Weinheim, Germany, 2007).
[2] J. C. Wyant and K. Creath, "Basic wavefront aberration theory for optical metrology", *Applied Optics and Optical Engineering* (Academic Press, San Diego, CA, 1992), Vol. 11, pp. 1–53.
[3] P. D. Burns and R. S. Berns, "Analysis multispectral image capture", *Proc. IS&T/SID 4th Color Imaging Conference* (IS&T, Springfield, VA, 1996), pp. 19–22.
[4] S. Tominaga, "Spectral imaging by a multi-channel camera", J. Electron. Imaging **8**, 332 (1999).
[5] H. Haneishi, T. Iwanami, T. Honma, N. Tsumura, and Y. Miyake, "Goniospectral imaging of three-dimensional objects", J. Imaging Sci. Technol. **45**, 451 (2001).
[6] S. Helling, E. Seidel, and W. Biehlig, "Algorithms for spectral color stimulus reconstruction with a seven-channel multispectral camera", *Proc. IS&T's 2nd European Conference on Color in Graphics, Imaging, and Vision* (IS&T, Springfield, VA, 2004), pp. 254–258.
[7] A. Mansouri, F. S. Marzani, J. Y. Hardeberg, and P. Gouton, "Optical calibration of a multispectral imaging system based on interference filters", Opt. Eng. **44**, 027004 (2005).

[8] A. Ribés, F. Schmitt, R. Pillay, and C. Lahanier, "Calibration and spectral reconstruction for CRISATEL: An art painting multispectral acquisition system", J. Imaging Sci. Technol. **49**, 563 (2005).
[9] J. Brauers, N. Schulte, A. A. Bell, and T. Aach, "Multispectral high dynamic range imaging", Proc. SPIE **6807**, 680704 (2008).
[10] J. Linhares, P. D. Pinto, and S. M. C. Nascimento, "The number of discernible colors in natural scenes", J. Opt. Soc. Am. A **25**, 2918 (2008).
[11] M. Vilaseca, R. Mercadal, J. Pujol, M. Arjona, M. de Lasarte, R. Huertas, M. Melgosa and F. H. Imai, "Characterization of the human iris spectral reflectance with a multispectral imaging system", Appl. Opt. **47**, 5622 (2008).
[12] J. Brauers, N. Schulte, and T. Aach, "Multispectral filter-wheel cameras: Geometric distortion model and compensation algorithms", IEEE Trans. Image Process. **17**, 2368 (2008).
[13] P. Urban, M. R. Rosen, and R. S. Berns, "Spectral image reconstruction using an edge preserving spatio-spectral Wiener estimation", J. Opt. Soc. Am. A **26**, 1868 (2009).
[14] M. Kozubek and P. Matula, "An efficient algorithm for measurement and correction of chromatic aberrations in fluorescence microscopy", J. Microsc. **200**, 206 (2000).
[15] T. Boult and G. Wolberg, "Correcting chromatic aberrations using image warping", *IEEE Computer Society Conference on Computer Vision and Pattern Recognition* (IEEE, Piscataway, NJ, 1992), pp. 684–687.
[16] R. Willson, "Modeling and calibration of automated zoom lenses", Proc. SPIE **2350**, 170–186 (1994).
[17] N. Joshi, R. Szeliski, and D. J. Kriegman, "PSF estimation using sharp edge prediction", *IEEE Conference on Computer Vision and Pattern Recognition* (IEEE, Piscataway, NJ, 2008), pp. 1–8.
[18] J. Mallon and P. Whelan, "Calibration and removal of lateral chromatic aberration in images", Pattern Recogn. Lett. **28**, 125 (2007).
[19] A. Conrady, "Decentering lens systems", Mon. Not. R. Astron. Soc. **79**, 384 (1919).
[20] D. C. Brown, "Decentering distortion of lenses", Photometric Eng. **32**, 444 (1966).
[21] J. Kang, H. Ok, J. Lim, and S.-D. Lee, "Chromatic aberration reduction through optical feature modeling", Proc. SPIE **7250**, 72500U (2009).
[22] S.-W. Chung, B.-K. Kim, and W.-J. Song, "Detecting and eliminating chromatic aberration in digital images", *IEEE International Conference on Image Processing (ICIP)* (IEEE, Piscataway, NJ, 2009), pp. 3905–3908.
[23] H. Kang, S.-H. Lee, J. Chang, and M. G. Kang, "Partial differential equation-based approach for removal of chromatic aberrations", J. Electron. Imaging **19**, 033016 (2010).
[24] S. B. Kang, "Automatic removal of chromatic aberration from a single image", *IEEE Conference on Computer Vision and Pattern Recognition* (IEEE, Piscataway, NJ, 2007), pp. 1–8.
[25] W. J. Smith, *Modern Optical Engineering* (McGraw-Hill, New York, 2000).
[26] M. Mühlich, and T. Aach, "High accuracy feature detection for camera calibration: A multi-steerable approach", *DAGM07: 29th Annual Symposium of the German Association for Pattern Recognition*, LNCS **4713**, 284–292 (2007).
[27] S. Hayakawa, "Zoom lens system", US Patent 2005/0068636 A1 (2005).
[28] J. Brauers and T. Aach, "Geometric calibration of lens and filter distortions for multi-spectral filter-wheel cameras", IEEE Trans. Image Process. **20**, 496 (2011).
[29] D. C. Brown, "Close-range camera calibration", Photogramm. Eng. **37**, 855 (1971).
[30] P. Deuflhard, *Newton Methods for Nonlinear Problems. Affine Invariance and Adaptive Algorithms*, Springer Series in Computational Mathematics, 2nd ed. (Springer, Berlin, Germany, 2006).
[31] R. Tsai, "A versatile camera calibration technique for high-accuracy 3D machine vision metrology using off-the-shelf TV cameras and lenses", IEEE J. Rob. Autom. **3**, 323 (1987).
[32] D. A. Forsyth and J. Ponce, *Computer Vision: A Modern Approach* (Prentice Hall, Upper Saddle River, NJ, 2002).
[33] K. Fukunaga, *Introduction to Statistical Pattern Recognition*, 2nd ed. (Academic Press, San Diego, CA 1990).
[34] A. N. Akansu and R. A. Haddad, *Multiresolution Signal Decomposition. Transforms, Subbands and Wavelets*, 2nd ed. (Academic Press, San Diego, CA, 2001).
[35] T. Aach, "Fourier, block and lapped transforms", *Advances in Imaging and Electron Physics*, edited by P. W. Hawkes, (Academic, San Diego, 2003), Vol. 128, pp. 1–52.